Journal of Sol-Gel Science and Technology (2026)118:64
https://doi.org/10.1007/s10971-026-07159-3

ORIGINAL PAPER

Sintering temperature driven structural and dielectric evolution of forsterite ceramics

Ahcene Keziz[1] · Menad Heraiz[1] · Linda Aissani[2] · Karam S. El-Nasser[3] · Ali Ismael[4] · Taha Abdel Mohaymen Taha[5]

Received: 31 December 2025 / Accepted: 9 March 2026

Abstract

This work reports the effect of sintering temperature (1400–1500 °C) on the structural, microstructural, and dielectric properties of forsterite (Mg_2SiO_4) ceramics synthesized via a sol-gel method. X-ray diffraction confirmed the formation of phase-pure orthorhombic forsterite 1500 °C, while samples sintered at 1400 °C contained 2.3 wt% MgO. Microstructural analysis revealed a density increase from 78%–88% and a reduction in open porosity from 17% to 9% with increasing sintering temperature. Impedance spectroscopy analysis identified hopping conduction as the dominant mechanism, with DC activation energy decreasing from ~1.12 eV to ~0.96 eV as the sintering temperature increased from 1400 - 1500 °C. The ceramics exhibited a low-frequency dielectric constant (ε_r) that increased with temperature. The results demonstrated that a sintering temperature of 1500 °C is optimal for achieving high density (2.88 g/cm³), reduced electrical activation energy, and superior microstructural properties, crucial for advanced electronic applications.

Graphical Abstract

Sol-gel forsterite ceramics sintered at 1400–1500 °C show improved density (78–88%) and reduced MgO impurities. Hopping conduction dominates; optimal 1500 °C yields high density (2.88 g/cm^3) and low activation energy (0.96 eV).

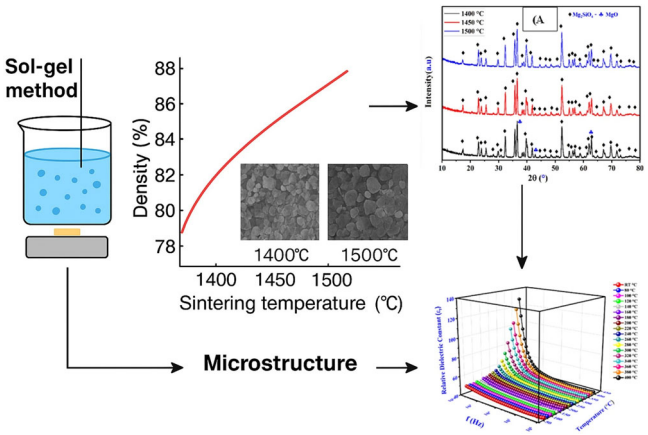

✉ Ahcene Keziz
ahcen.keziz@univ-msila.dz

✉ Ali Ismael
k.ismael@lancaster.ac.uk

✉ Taha Abdel Mohaymen Taha
taha.hemida@yahoo.com

[1] Department of Physics, Physics and Chemistry of Materials Laboratory, University pole, 28000 M'sila, Algeria

[2] Mater science department, ABBES Laghrour- Khenchela, Khenchela P.O 1252 40004, Algeria

[3] Department of Chemistry, College of Science, Jouf University, Sakaka, Aljouf 72341, Saudi Arabia

[4] Physics Department, Lancaster University, Lancaster LA1 4YB, UK

[5] Physics and Engineering Mathematics Department, Faculty of Electronic Engineering, Menoufia University, Menouf 32952, Egypt

Published online: 02 June 2026

Keywords Forsterite (Mg_2SiO_4) · Rietveld-refinement · Complex impedance spectroscopy · Relative dielectric constant · Non-Debye relaxation

Highlights

- Optimal sintering at 1450 °C yields phase-pure orthorhombic forsterite ceramics.
- Densification improved, reducing porosity from 17% to 9.3% with 88% density.
- Ceramics showed stable dielectric properties ideal for electronic substrates.
- Electrical response is grain-dominated with non-Debye hopping conduction.

1 Introduction

The MgO–SiO_2 system comprises several important phases, such as magnesium metasilicate ($MgSiO_3$) with enstatite type structure, MgO with periclase type structure, and silica SiO_2; however, magnesium orthosilicate (Mg_2SiO_4) with forsterite type structure uniquely stands out because of its exceptional combination of compositional precision and multifunctional properties. Its stoichiometric composition (57.29 wt% MgO and 42.71 wt% SiO_2) is critical, as even slight deviations that generate secondary phases can severely deteriorate performance, particularly its outstanding dielectric behavior [1–4]. Forsterite exhibits a moderate relative permittivity ($\varepsilon_r \approx 6$–7), ideal for maintaining signal integrity, together with an extremely high Q factor ($Q \times f \approx 240{,}000$ GHz), indicating minimal dielectric loss and making it a benchmark material for high-frequency substrates, microwave dielectrics, and laser components [5–8]. In addition to its dielectric excellence, forsterite demonstrates remarkable thermo-mechanical properties, including a high melting point (~1890 °C), excellent thermal stability, low thermal expansion that mitigates thermal stresses, and high hardness (~7.68 GPa), all of which underpin its suitability for refractory, coating, composite, and electronic packaging applications [9–12]. Beyond engineering uses, forsterite also exhibits notable bioactivity; its controlled dissolution and release of Mg^{2+} and Si^{4+} ions promote bone cell adhesion, proliferation, and apatite formation, highlighting its strong potential for bone grafts, scaffolds, and orthopedic implant coatings [13–15].

The various synthesis techniques for forsterite represent complementary strategies to address its primary challenge: the intrinsically high formation temperature (>1400 °C) required for solid-state reactions between MgO and SiO_2, which typically results in coarse powders, chemical inhomogeneity, and high energy consumption. While the conventional solid-state route remains a baseline approach, it demands repeated grinding and prolonged high-temperature treatments and often suffers from impurity formation [7]. In contrast, wet-chemical and soft-chemistry methods such as sol–gel [13], co-precipitation [6], polymer precursor [7], and hydrothermal techniques [14] promote molecular-level mixing of magnesium and silicon precursors, significantly enhancing reactivity, lowering synthesis and calcination temperatures, and yielding ultrafine, homogeneous, high-purity powders with superior sinterability. Energy-efficient alternatives, including auto-combustion [1] and mechanical activation [15], further reduce thermal requirements by generating internal heat through exothermic redox reactions or by increasing defect density and surface area via high-energy ball milling. Regardless of the synthesis route, sintering temperature remains a critical processing parameter, as it directly governs densification and grain growth; eliminating porosity is essential to achieving high mechanical strength and minimizing dielectric loss (maximizing Q), while grain growth must be carefully controlled to avoid microstructural degradation [16, 17]. From a dielectric performance standpoint, a fine, uniform, and dense microstructure is generally optimal for achieving low loss and stable permittivity, making precise tailoring of the sintering profile crucial for optimizing ε_r and Q. Additionally, the use of sintering aids such as B_2O_3, V_2O_5, or Li_2CO_3 can markedly enhance densification at reduced temperatures by forming transient liquid phases, but their content must be carefully optimized to avoid the formation of lossy secondary phases at grain boundaries that would compromise the exceptional dielectric Q factor of forsterite [18, 19].

Despite the extensive investigations into forsterite ceramics, several research gaps remain unresolved. Although numerous synthesis routes have been explored to reduce calcination temperatures and enhance purity, there is still limited understanding of how microstructural evolution particularly grain growth dynamics and grain boundary chemistry directly governs the dielectric and conduction behavior across wide frequency ranges. Existing studies widely acknowledge the significance of sintering temperature, yet systematic correlations between sintering-induced microstructural transitions and frequency-dependent dielectric responses remain insufficiently addressed. Moreover, the interplay between grain interior and grain boundary contributions to AC conductivity, as well as the mechanisms driving hopping behavior, require deeper clarification through combined structural, microstructural, and electrical analyses. Therefore, a comprehensive,

temperature-dependent investigation linking phase purity, grain development, and dielectric performance is essential to bridge these gaps and optimize forsterite ceramics for advanced electronic applications.

Herein in this article, we investigate the effect of sintering temperature on structural, and dielectric and properties of forsterite (Mg_2SiO_4) ceramics. This study focuses on the synthesis of forsterite (Mg_2SiO_4) precursor powder via the sol-gel method using tetraethyl orthosilicate (TEOS) and magnesium nitrate hexahydrate ($Mg(NO_3)_2{\cdot}6H_2O$) as starting materials, with detailed characterization of samples sintered at 1400, 1450 and 1500 °C for 2 h. X-ray diffraction (XRD) analysis confirmed the formation of phase-pure orthorhombic forsterite (space group *Pbnm*) with high crystallinity. Field-emission scanning electron microscopy (FESEM) revealed a well-defined microstructure characterized by distinct grains separated by grain boundaries. Grain boundaries were clearly resolved, with energy-dispersive spectroscopy (EDS) verifying stoichiometric Mg_2SiO_4 composition. This work further investigated the dielectric and AC conductivity properties of sintered pellets across a wide frequency range (0.1 kHz–1 MHz). Frequency-dependent permittivity and loss tangent trends correlated with microstructural features observed in SEM, where grain boundary effects dominated low-frequency responses while bulk contributions prevailed at higher frequencies. AC conductivity analysis, supported by Jonscher's power law, identified hopping conduction as the dominant mechanism, with activation energies derived from Arrhenius plots.

2 Materials and methods

2.1 Materials

Magnesium nitrate hexahydrate ($Mg(NO_3)_2{\cdot}6H_2O$, ≥99.8% purity) was procured from Biochem Chemopharma (Georgia, USA), serving as the magnesium source for the synthesis. Tetraethyl orthosilicate (TEOS, $Si(C_2H_5O)_4$, 99% purity) was obtained from Fluka and acted as the silicon precursor, while absolute ethanol (CH_3CH_2OH, ≥99.8% purity) from Sigma-Aldrich was used as the solvent. These high-purity reagents were deliberately selected to minimize impurities that could affect the synthesis process or the final properties of the forsterite material.

2.2 Processing of powders

Forsterite precursor powders were synthesized via a sol–gel route using tetraethyl orthosilicate (TEOS) and magnesium nitrate hexahydrate and magnesium nitrate hexahydrate as silicon and magnesium sources, respectively. TEOS was dissolved in ethanol at a volumetric ratio of TEOS: ethanol = 1:4, while and magnesium nitrate hexahydrate was separately dissolved in deionized water at TEOS: water = 1:20. Each solution was magnetically stirred for 30 min to ensure complete homogenization prior to mixing [13]. Subsequently, diluted nitric acid (HNO_3, 0.1 M) was gradually added to the mixture under continuous magnetic stirring for 2 h at room temperature until a transparent and homogeneous solution was obtained. Nitric acid plays a key role in accelerating hydrolysis and condensation reactions, thereby promoting the formation of a highly homogeneous gel network. The acidic oxidizing medium also facilitates the removal of residual organic groups and solvents, reducing carbon residues and enhancing crystalline purity after calcination. Furthermore, it promotes the homogeneous reaction between Mg^{2+} ions and silica (SiO_2) and suppresses the formation of undesirable secondary phases such as MgO or free silica. The resulting sol was aged at 60 °C for 48 h to induce gelation. The obtained gel was dried at 120 °C for 24 h to remove residual solvents, yielding a yellowish precursor powder. The dried powder was manually ground using an agate mortar and pestle to reduce agglomeration and then uniaxially cold-pressed into pellets. Finally, the samples were calcined and sintered at 1400, 1450, and 1500 °C for 2 h to obtain crystalline forsterite and achieve densification. This optimized protocol ensures high phase purity and a controlled microstructure, which are essential for tailoring the electrical and mechanical properties of the material.

2.3 Sample sintering

Cylindrical samples (13 mm in diameter and ~4 mm in height) were prepared from the previously synthesized powders using a hardened steel mold. The powders were uniaxially pressed under 150 MPa using a hydrostatic press, with the samples held under pressure for a specified duration to ensure uniform stress distribution. An air pump was employed to remove trapped air during pressing. The compacted samples were then sintered at 1400, 1450, and 1500 °C in an electric muffle furnace (Nabertherm) equipped with an automated program for precise temperature and time control. The heating rate was 5 °C/min until the target temperature was reached, maintained for 2 h, followed by cooling at the same rate to room temperature before sample removal.

2.4 Characterization and analysis

Phase purity, crystallinity, and crystal structure were systematically evaluated using high-resolution X-ray diffraction (XRD), employing a PANalytical X'Pert Pro diffractometer with Cu Kα radiation ($\lambda = 1.5418$ Å)

operated at 40 kV and 30 mA. Data were collected over a 2θ range of 10–80° with a step size of 0.02° and a scan time of 30 min per sample, which provides an optimal balance of intensity and resolution for oxide ceramics. Quantitative phase analysis was carried out using Rietveld refinement, the benchmark method for structural characterization, enabling precise determination of lattice parameters, estimation of crystallite size through peak-broadening analysis, and assessment of microstrain; any deviation in the refined unit cell constants serves as a sensitive indicator of non-stoichiometry, residual stress, or possible dopant incorporation. Complementary microstructural and compositional analyses were performed using field-emission scanning electron microscopy (FESEM) equipped with energy-dispersive spectroscopy (EDS) (QUANTA 250 FEG), where the field emission gun ensured superior spatial resolution and clear visualization of grain surfaces and boundaries. FESEM analysis provided detailed insight into grain size and distribution, grain morphology, porosity, and the cleanliness of grain boundaries, all of which are critical factors influencing dielectric loss. EDS point analysis and elemental mapping verified the expected stoichiometry (Mg:Si:O ≈ 2:1:4), assessed elemental homogeneity, and detected any incidental impurities or segregated sintering aids at grain boundaries. For dielectric measurements, sintered samples were prepared as pellets with standardized dimensions (~12 mm diameter and ~1.5 mm thickness) and coated on both faces with silver paste to form parallel-plate capacitor electrodes, ensuring reliable electrical contact and accurate determination of intrinsic dielectric parameters. The electrical response was investigated using Solartron impedance spectroscopy (IS), the core technique for deconvoluting the contributions of grains, grain boundaries, and electrode interfaces, over a broad frequency range (0.1 kHz–1 MHz) and temperature interval (40–400 °C) an applied AC voltage of 50 mV, where frequency sweeps distinguish slow interfacial and space-charge processes from fast intrinsic polarizations, and temperature variation activates thermally driven conduction and relaxation mechanisms.

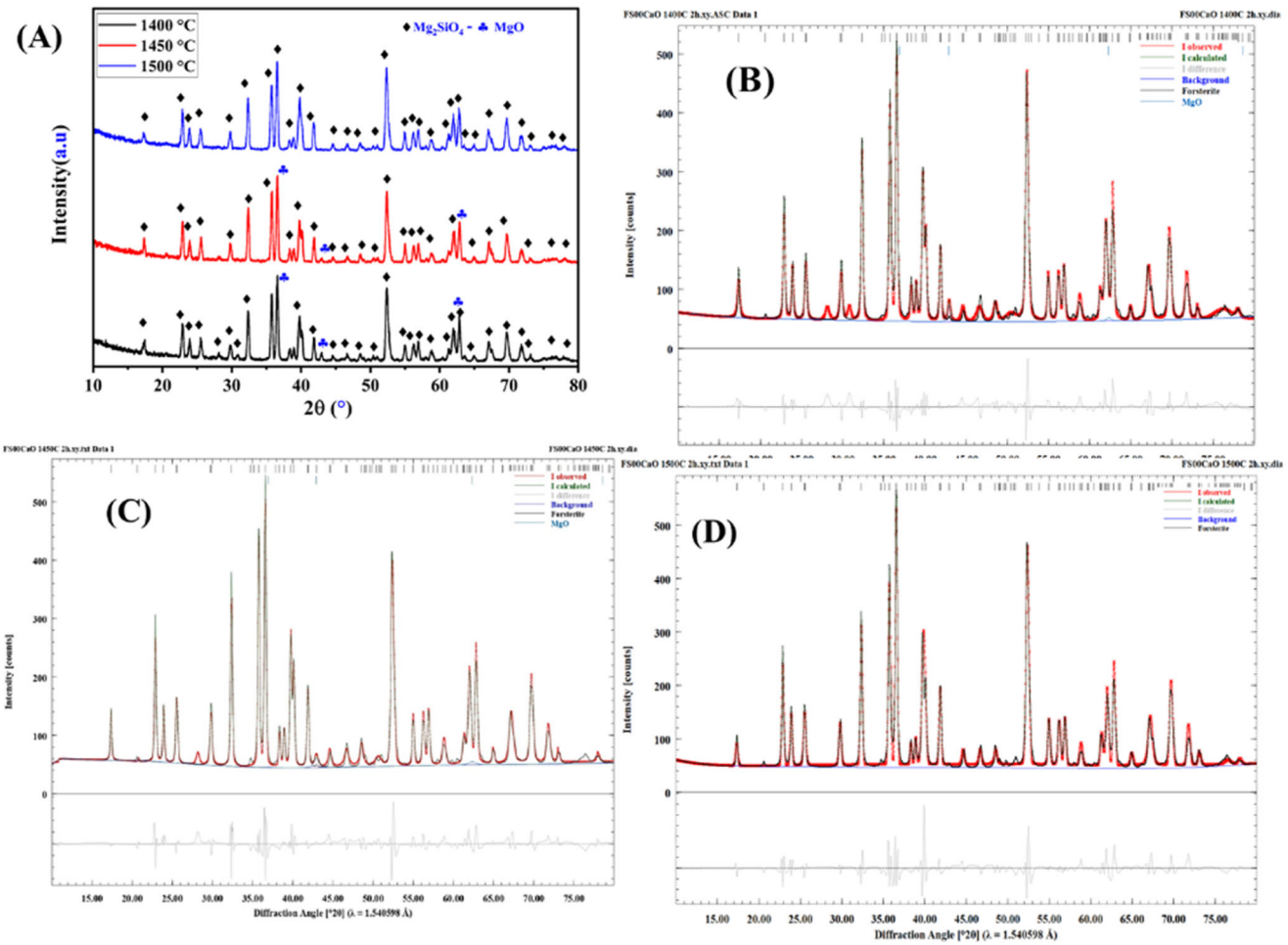

Fig. 1 **A** XRD spectra of forsterite sintered for 2 h at 1400, 1450, and 1500 °C, **B–D** the structural characteristics of the sintered forsterite samples

3 Results and discussion

3.1 XRD analysis

The phase purity of forsterite (Mg_2SiO_4) prepared via the sol–gel method and sintered at 1400, 1450, and 1500 °C for 2 h was investigated using X-ray powder diffraction (XRD), as shown in Fig. 1A. The XRD patterns of the samples sintered at 1400 and 1450 °C show reflections from both the forsterite phase and MgO, with a notable decrease in MgO reflection intensity at 1450 °C. In contrast, the sample sintered at 1500 °C for 2 h exhibits reflections corresponding exclusively to the forsterite phase, indicating the completion of the crystallization process and the elimination of secondary phases at the higher sintering temperature. Figure 1B–D present the Rietveld refinement of the XRD patterns for the samples sintered at 1400, 1450, and 1500 °C, respectively. Solid lines represent the calculated diffraction intensities, whereas crosses correspond to the experimental data. The difference between the calculated and experimental intensities is displayed above each profile, allowing an accurate assessment of the refinement quality.

The Bragg peak positions corresponding to each identified phase—forsterite and magnesium oxide for the samples sintered at 1400 and 1450 °C, and forsterite only for the sample sintered at 1500 °C are marked above the picks in the patterns as shown in Fig. 2A–C. All sintered Mg_2SiO_4 samples crystallized in an orthorhombic structure belonging to the Pbnm space group. Structural parameters derived from the Rietveld analysis of the sintered forsterite are

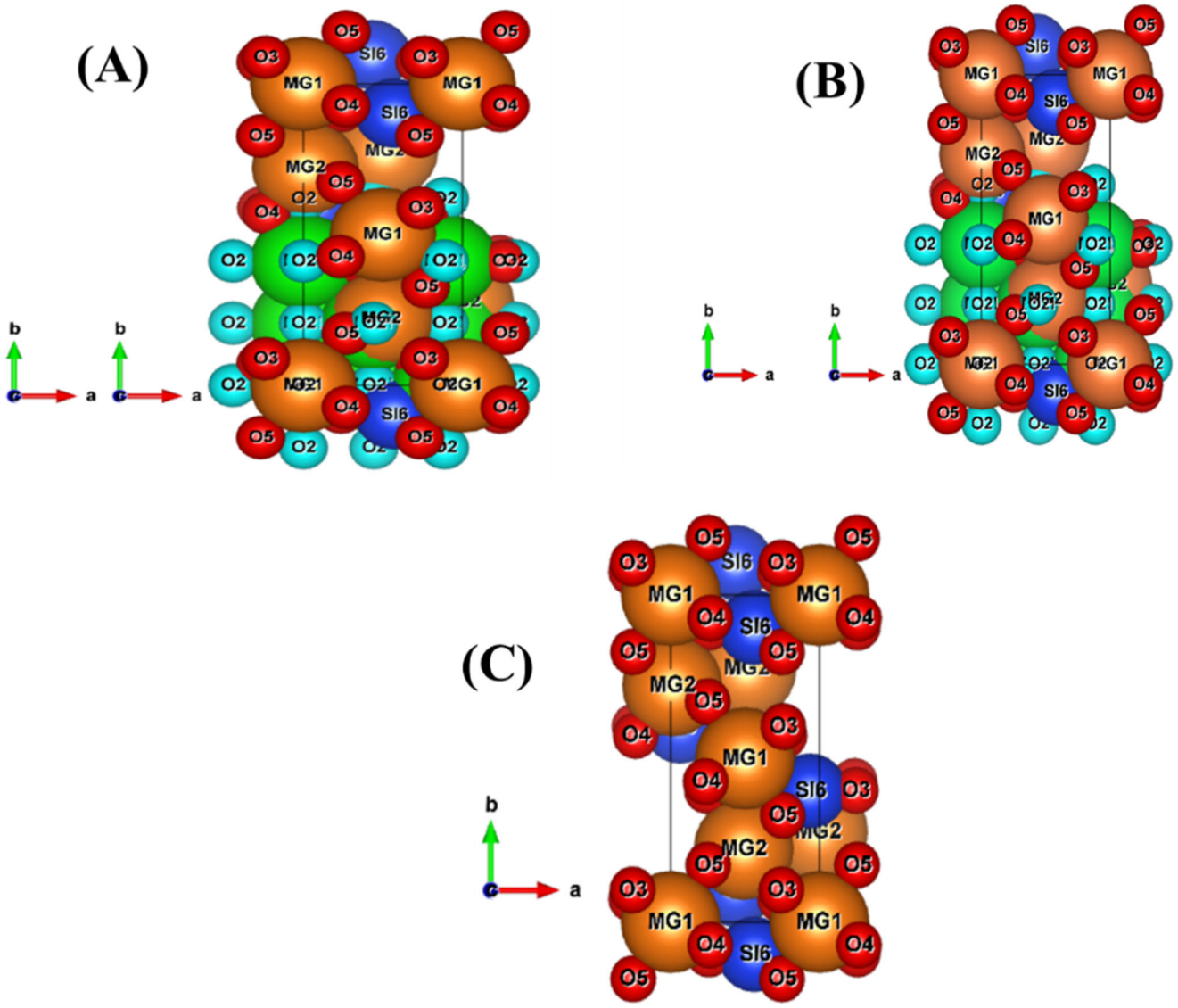

Fig. 2 The mutual arrangement of the structural elements of the unit cell in different projections for samples sintered at **A**) 1400, **B**) 1450, and **C**) 1500 °C.

Table 1 The structural characteristics of the forsterite heat-treated sample at 1400 °C

Phase Formula	Forsterite # Mg_2SiO_4					
Lattice parameters	Space group: P b n m, a = 4.74930 ± 0.00035 (Å) ; b = 10.20902 ± 0. 00077 (Å); c = 5.98276 ± 0.00044 (Å); α = β = γ = 90∘; V = 290.078287Å^3					
Reliability factors	Rwp = 8.43%; Rexp = 11.40%; χ^2 = 0.5352					
	x	y	z	B	Occupancy	Site
Mg (1)	0.00000	0.00000	0.00000	−0.000	1	4a
Mg (2)	0.98840	0.27730	0.25000	0.776	1	4c
O (3)	0.76290	0.08840	0.25000	3.683	1	4c
O (4)	0.23280	0.42740	0.25000	−0.000	1	4c
O (5)	0.26880	0.17290	0.01560	0.855	1	8d
Si (6)	0.42990	0.09746	0.25000	0.292	1	4c
Magnesium Oxide (Periclase) "MgO"						
	Space group: F m −3 m, a = b = c = 4.2124 ± 0.00019 (Å); α = β = γ = 90∘; V = 74.746145 Å^3					
Mg (1)	0.00000	0.00000	0.00000	9.602	1	4a
O (2)	0.50000	0.50000	0.50000	0.000	1	4b
Refined Chemical Composition						
	Forsterite			MgO		
Phase Quantity (wt-%)	97.70			2.30		

Table 2 The structural characteristics of the forsterite heat-treated sample at 1450 °C

Phase Formula	Forsterite # Mg_2SiO_4					
Lattice parameters	Space group: P b n m, a = 4.748871 ± 0.00041 (Å); b = 10.20408 ± 0. 00079 (Å); c = 5.98162 ± 0.00044 (Å); α = β = γ = 90∘; V = 289.846666Å^3					
Reliability factors	Rwp = 7.90%; Rexp = 11.35%; χ^2 = 0.4845					
	x	y	z	B	Occupancy	Site
Mg (1)	0.00000	0.00000	0.00000	0.148	1	4a
Mg (2)	0.99400	0.27529	0.25000	1.470	1	4c
O (3)	0.75000	0.09510	0.25000	4.034	1	4c
O (4)	0.24170	0.42960	0.25000	0.987	1	4c
O (5)	0.26530	0.16990	0.01560	1.301	1	8d
Si (6)	0.42520	0.09551	0.25000	0.731	1	4c
Magnesium Oxide (Periclase) "MgO"						
	Space group: F m −3 m, a = b = c = 4.2123 ± 0.00040 (Å); α = β = γ = 90∘; V = 74.740815 Å^3					
Mg (1)	0.00000	0.00000	0.00000	2.000	1	4a
O (2)	0.50000	0.50000	0.50000	0.000	1	4b
Refined Chemical Composition						
	Forsterite			MgO		
Phase Quantity (wt-%)	98.51			01.49		

summarized in Tables 1–3. The Profex program, in combination with Vesta, was used to extract the structural data, including lattice parameters and unit cell volumes, enabling evaluation of phase purity, grain size, and possible secondary phases [20, 21].

3.2 Microstructure analysis

The SEM micrographs of forsterite pellets sintered at 1400, 1450, and 1500 °C for 2 h are presented in Fig. 3A–C **respectively**, reveal a well-defined microstructure

Table 3 The structural characteristics of the forsterite heat-treated sample at 1500 °C

Phase Formula	Forsterite # Mg_2SiO_4					
Lattice parameters	Space group: P b n m, a = 4.75161 ± 0.00038 (Å); b = 10.21060 ± 0. 00078 (Å); c = 5.98235 ± 0.00046 (Å); α = β = γ = 90∘; V = 290.244392 $Å^3$					
Reliability factors	Rwp = 9.71%; Rexp = 11.57%; $\chi^2 = 0.7043$					
	x	y	z	B	Occupancy	Site
Mg (1)	0.00000	0.00000	0.00000	1.035	1	4a
Mg (2)	0.99010	0.27620	0.25000	2.902	1	4c
O (3)	0.74390	0.09760	0.25000	6.301	1	4c
O (4)	0.23570	0.42950	0.25000	0.675	1	4c
O (5)	0.25240	0.17379	0.01190	2.483	1	8d
Si (6)	0.43720	0.09926	0.25000	1.897	1	4c
Refined Chemical Composition						
	Forsterite			MgO		
Phase Quantity (wt-%)	100			00		

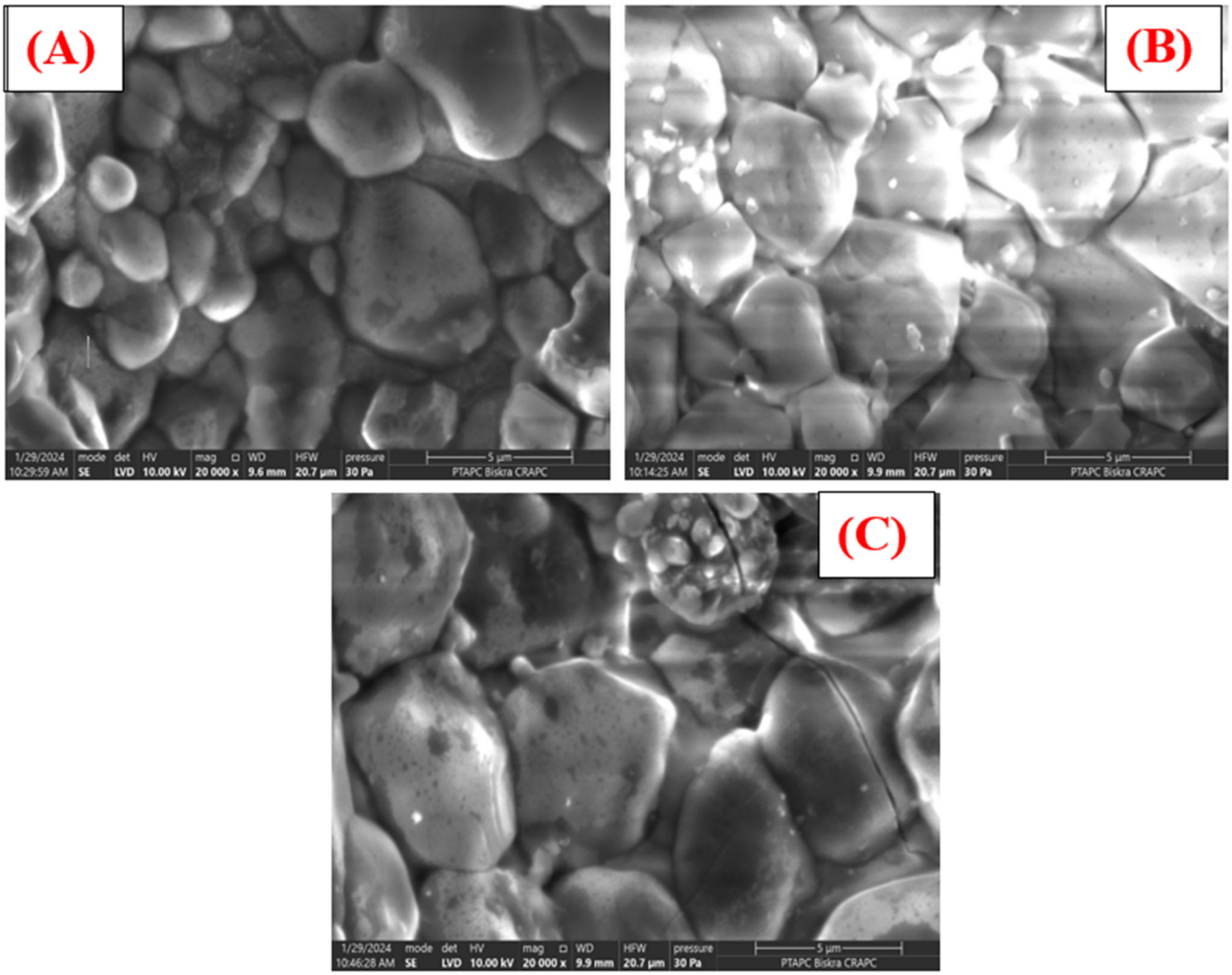

Fig. 3 The SEM micrographs of the sintered forsterite samples at **A**)1400, **B**)1450, and **C**)1500 °C

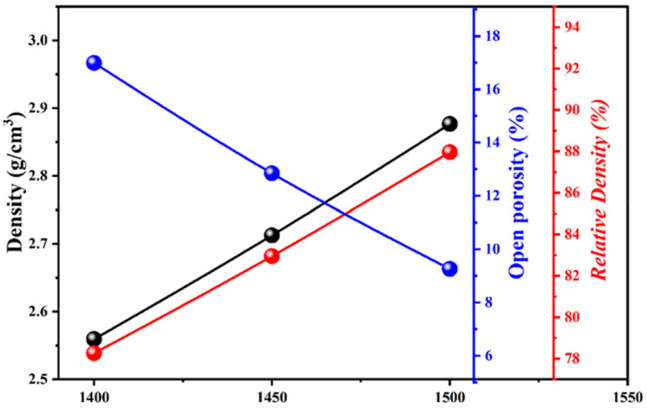

Fig. 4 Density, relative density, and open porosity of forsterite sintered at various temperatures

Table 4 Density ρ (g/cm^3), relative density (%), and open porosity (%) of forsterite sintered for 2 h at various temperatures

ρ	Open porosity	Relative density	ρ	Open porosity	Relative density	ρ	Open porosity	Relative density
	1400 °C			1450 °C			1500 °C	
2.56	16.99	78.27	2.7126	12.84	82.95	2.8765	9.26	87.97

characterized by distinct grains separated by grain boundaries. The images depict a dense arrangement of forsterite granules with varying shapes and sizes, indicating a heterogeneous morphology. The average grain size was found to grow as the sintering temperature rose. This indicates that big grains formed as a result of the crystallite diffusing. Consequently, microscopic grains that are irregular in size and form, irregularly aligned, and closely related compose SEM images.

3.3 Apparent porosity and bulk density

In order to measure both the density $\boldsymbol{\rho}$ (g/cm^3), open porosity (%), and relative density for of the sintered forsterite ($\mathbf{Mg_2SiO_4}$) samples at 1400, 1450, and 1500 °C for 2 h, the following equations served as the foundation for our application of the Archimedes approach [22, 23]:

$$m_2 = m_1 + \rho_{H_2O*} V_{po}. \quad (1)$$

$$m_3 = m_1 - (V_T - V_{po})\rho_{H_2O}. \quad (2)$$

$$(V_T - V_{po}) = \frac{(m_1 - m_3)}{\rho_{H_2O}}. \quad (3)$$

$$\rho = \frac{m}{V_T} = \frac{m_1}{m_2 - m_3} \times \rho_{H_2O}. \quad (4)$$

$$V_{po} = \frac{(m_2 - m_1)}{\rho_{H_2O}}. \quad (5)$$

$$X_{V_{po}}\% = \frac{V_{po}}{V_T} \times 100 = \frac{m_2 - m_1}{m_2 - m_3} \times 100. \quad (6)$$

where ρ represents density, m_1 the mass of sample in air, m_2 the mass of the sample after it has been emptied of air, V_T is the total volume, and (V_{op}) is the volume of open pores. The ratio of the measured and theoretical densities is used to determine the relative density (densification) of the sintered forsterite.

Figure 4 and Table 4 show the density ρ (g/cm3), open porosity (%), and relative density (%) of forsterite that was sintered for two hours at various temperatures (1400, 1450, and 1500 °C) without being subjected to grinding. It is easily observable from Fig. 4 that the open porosity decreases with the increase in sintering temperature from 1400 to 1500 °C. This decrease is accompanied with an increase in both the density and relative density as seen in Fig. 4. The better densification caused by enhanced diffusion is the reason for the decreases in open porosity and increases in density and relative density as the sintering temperature rises. This is because diffusion primarily regulates the thermally activated process of sintering. Consequently, the diffusion percentage and the percentage of pores eliminated increase with increasing sintering temperature [24, 25]. However, the relative density measurements show that the forsterite sintered samples are not 100% dense since they still have some closed pores. For instance, a forsterite sample sintered for 2 h at 1500 °C had a relative density of 87.97% and an open porosity of 9.26%.

3.4 Impedance analyses

The electrical properties of forsterite samples obtained using a sol-gel process that were thermally treated by sintered at 1400, 1450, and 1500 °C for two hours were examined using complex impedance spectroscopy.

The variation of the real part of impedance (Z′) for forsterite sintered at 1400, 1450, and 1500 °C for 2 h with range frequency (10^2–10^6 Hz) at various temperatures (from 40 to 400 °C) are plotted in Fig. 5A–C, **respectively**. Evidently, for all sintered samples the real part impedance (Z′) decreases as the temperature and frequency drops, indicating a rise in the AC conductivity [26, 27]. The real component of impedance (Z′) values at lower frequencies decrease as the temperature rises, exhibiting behavior similar to those of ceramics [28], bioceramics [29], PZT [30] and semiconductors [31]. The real part of the impedance (Z′) converges and becomes nearly independent of frequency in the high-frequency region at all measured temperatures. This behavior can be attributed to the reduction of potential barrier effects within the material, which weakens space-charge polarization and enhances the mobility of charge carriers [32].

The variation of imaginary part of impedance (-Z″) for sintered forsterite samples with range frequency (10^2–10^6 Hz) at room temperature to 400 °C are depicted in Fig. 6A–C, **respectively**. One observes a big, asymmetrical peak. The imaginary part of the impedance (-Z″) increased in value as the frequencies increased. Achieving a maximum value ($-Z''m_{ax}$), additionally, as the temperature increases, the maximum value ($-Z''m_{ax}$) of imaginary part rises to higher frequencies, proving that the relaxation time in the forsterite samples is temperature dependent [1, 33].

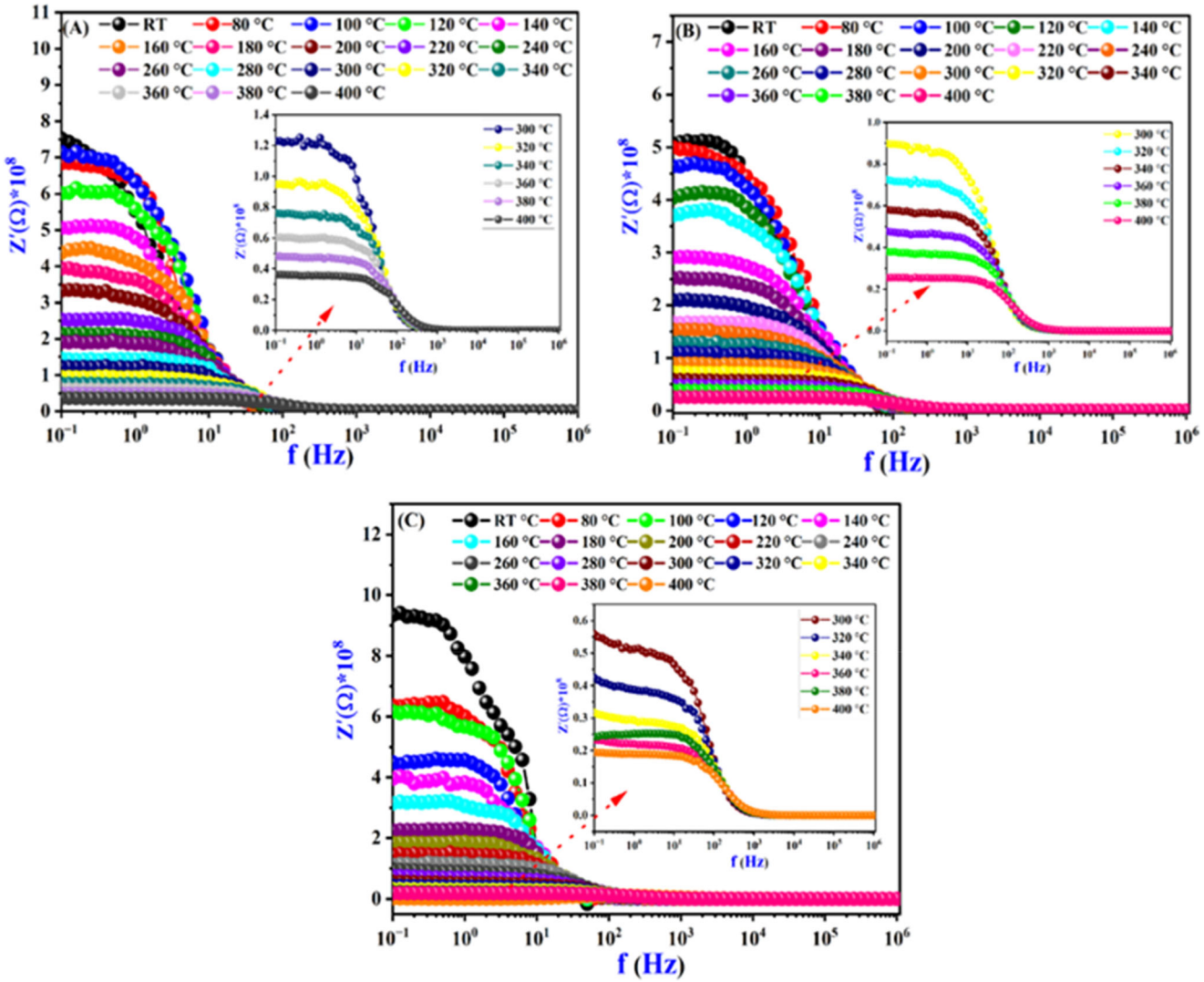

Fig. 5 The real part of impedance (Z′) versus frequency for the forsterite samples sintered at **A**) 1400, **B**) 1450, and **C**) 1500 °C.

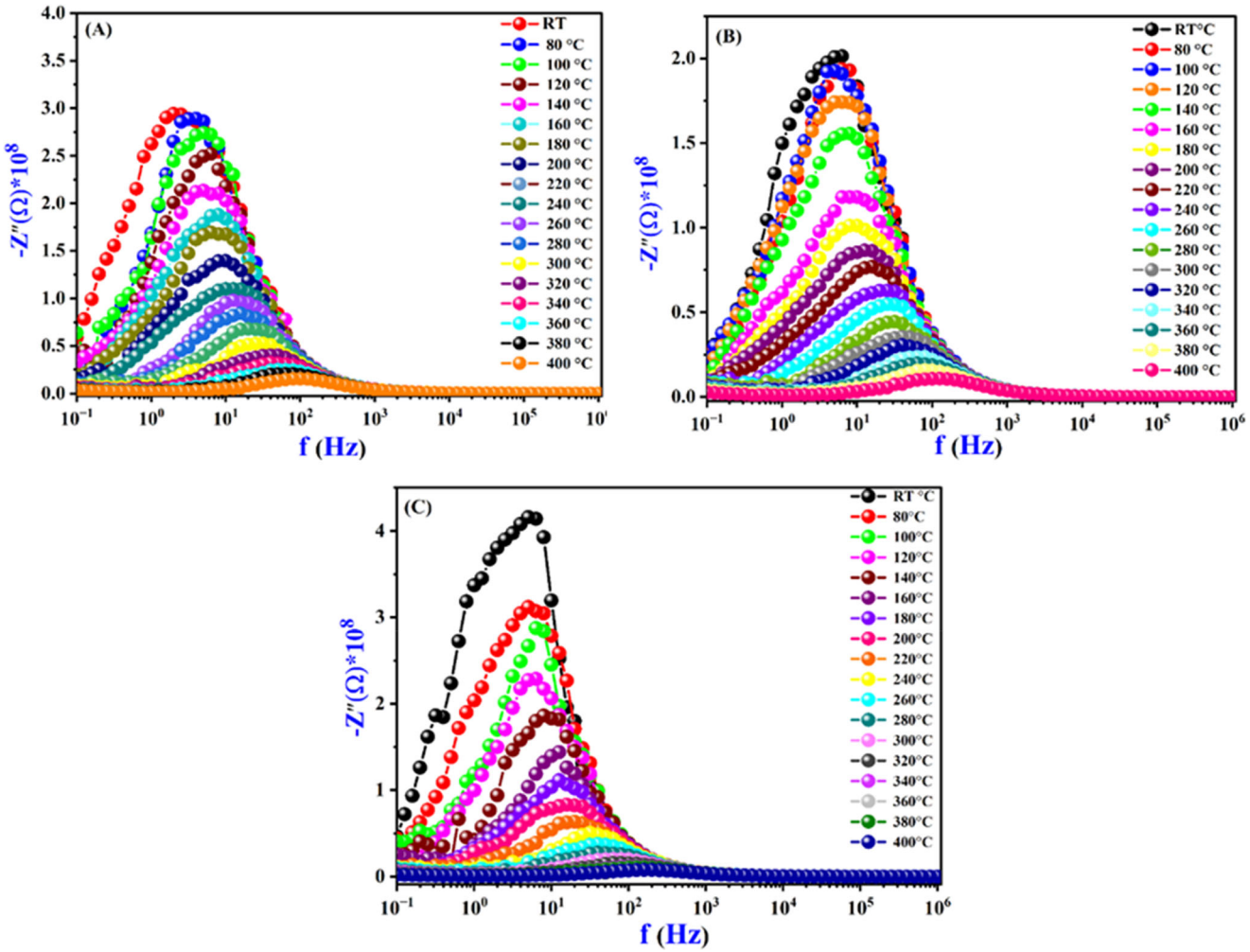

Fig. 6 Graphs of the imaginary part of impedance (-Z″) versus frequency for forsterite sintered at **A**) 1400, **B**) 1450, and **C**) 1500 °C for 2 h

One useful, non-destructive method for evaluating a material's electrical characteristics is impedance spectroscopy (IS). Typical Nyquist plots or complex impedance spectra for forsterite samples sintered at 1400, 1450, and 1500 °C for 2 h at various temperatures are shown in Fig. 7A–C, respectively [1, 33–35]. The Nyquist plots exhibit a semicircular arc. As the temperature rises, the semi-circular arc's radius decreases. The latter phenomenon is ascribed to the only existence of electrical relaxation processes and suggests non-Debye type behavior within the forsterite samples being studied [34, 35]. At higher temperatures, the effect of temperature on impedance behavior becomes more evident. It's noteworthy that the presence of an only semicircular arc indicates the dominance of the grain's contribution [34, 35].

3.5 Electrical conductivity

In order to ascertain electrical conductivity behavior of sintered forsterite at 1400, 1450, and 1500 °C for 2 h with range frequency ($10^{2-}10^{6}$ Hz) at various temperatures, the following Eq. (8) was utilized to calculate the electrical conductivity (σ) utilizing the measurements given by impedance spectroscopy [36]**:**

$$\sigma = \frac{t}{A}\frac{(Z')}{\left(Z''^2 + Z'^2\right)} \tag{7}$$

where A and t are the area and thickness of the forsterite samples.

The behavior of electrical conductivity with frequency for forsterite samples sintered at 1400, 1450, and 1500 °C for two hours at different temperatures is shown in Fig. 8A–C. The electrical conductivity exhibits two distinct tendencies. For lower frequencies, the electrical conductivity value is stable and appear as a plateau. This plateau demonstrates the direct current conductivity (σ_{dc}) of the sintered forsterite [36]. The second part shows following the plateau at high frequencies. It depicts a variation in the trend of the electrical conductivity (σ_{ac}) with change of frequency.

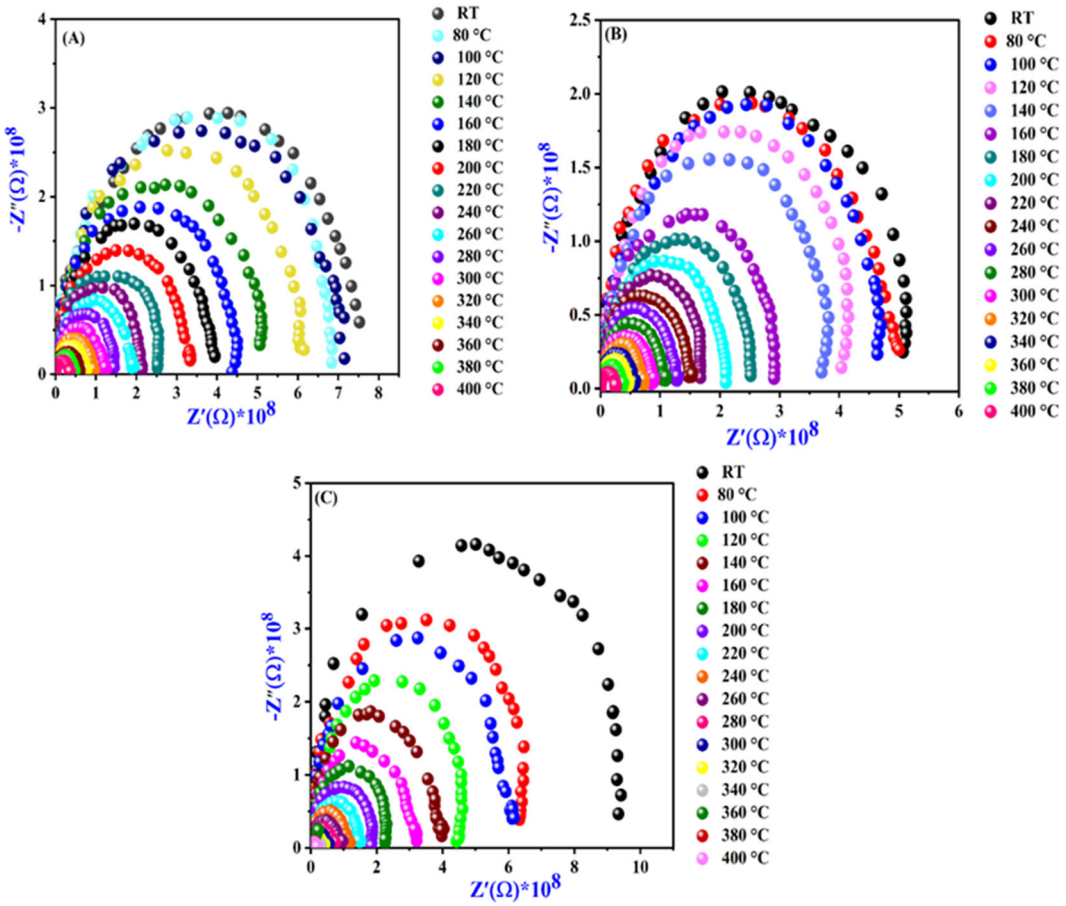

Fig. 7 Graphs of the Nyquist curves (-Z″ vs. Z′) for forsterite sintered at **A**) 1400, **B**) 1450, and **C**) 1500 °C for 2 h

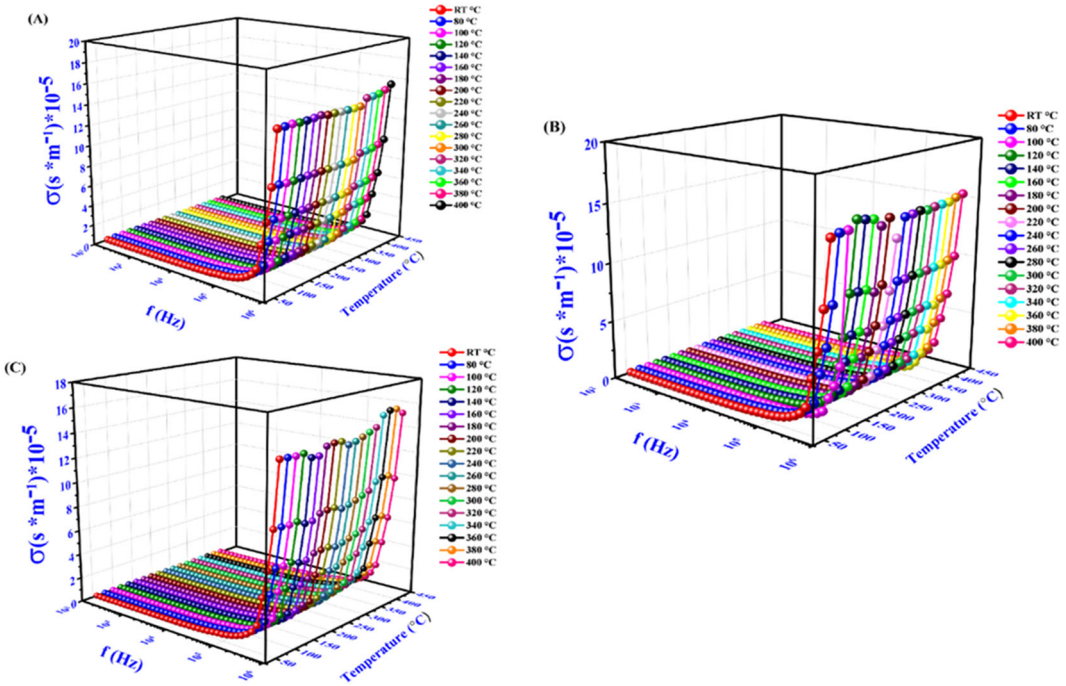

Fig. 8 The dependence of electrical conductivity behavior with frequency for forsterite samples sintered at **A)** 1400, **B)** 1450, and **C)** 1500 °C for 2 h

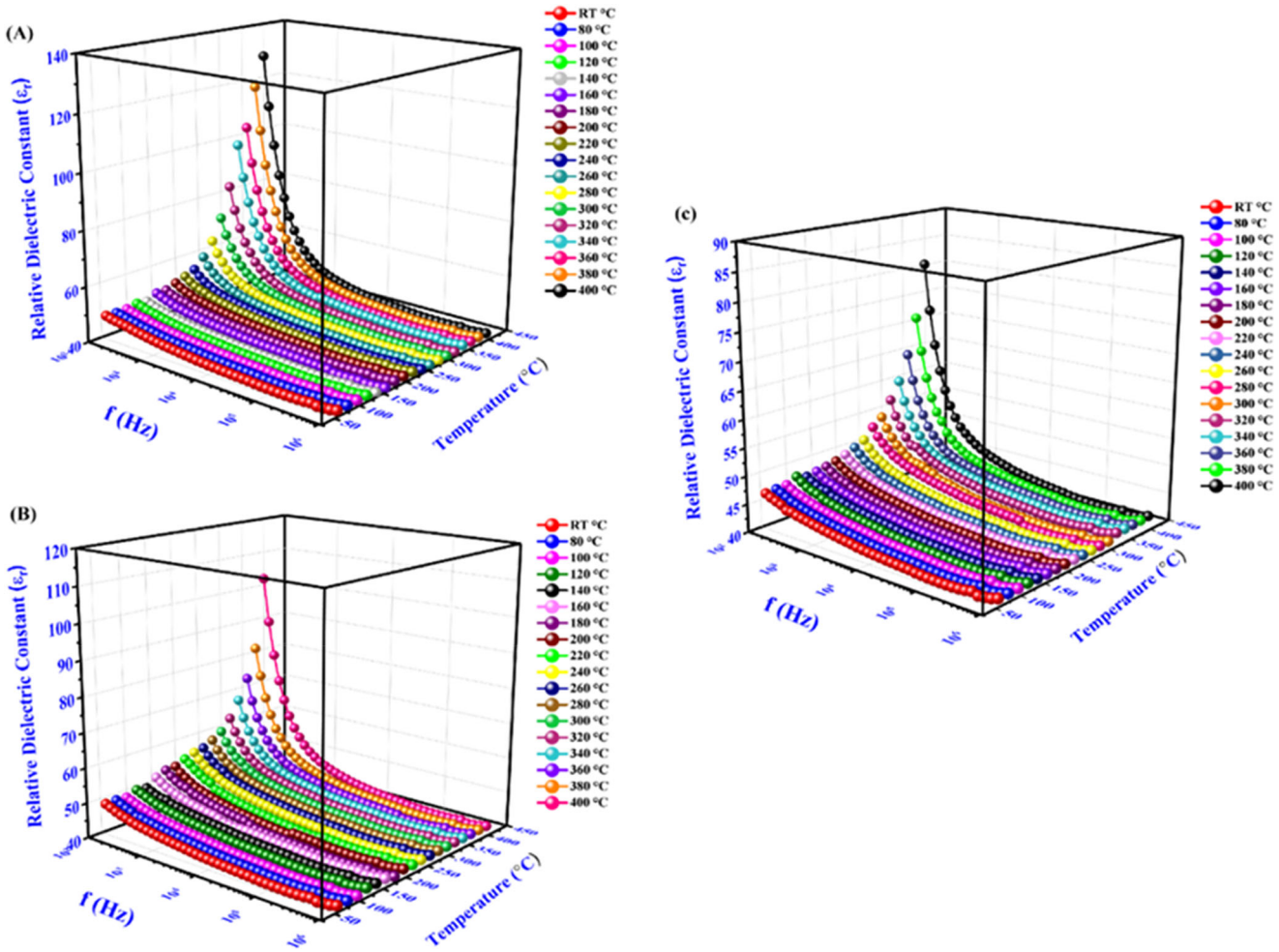

Fig. 9 The plots of relative dielectric constant at various temperatures for sintered forsterite samples at **A**) 1400, **B**) 1450, and **C**) 1500 °C

This can be explained by a different conduction mechanism from that of the plateau region [37]. σ_{dc} corresponds to the low-frequency conductivity because only at low frequencies do charge carriers have sufficient time to undergo long-range transport and contribute to a steady current. At higher frequencies, carrier motion becomes localized and contributes only to AC conductivity.

At high frequencies, the conductivity dispersion phenomena are commonly interpreted using Jonscher's law [38, 39]. When the frequency changes, it explains how the electrical conductivity of forsterite changes. Jonscher's law states that the electrical conductivity (σ) of a forsterite can be expressed as in Eq. (10) [40, 41]**:**

$$\sigma = \sigma_{dc} + A\omega^{S} \tag{8}$$

where ω is the angular frequency, σ_{dc} is the temperature-dependent low-frequency conductivity, A is the temperature-dependent coefficient, and s represents the degree of interaction between mobile charge carriers and their surroundings.

3.6 Dielectric analyses

3.6.1 Frequency dependent dielectric characterization

A solid material's dielectric behavior can be explained by the relative dielectric constant (ε_r), the following method can be used to calculate the relative dielectric permittivity (ε_r) from capacitance data [42]:

$$\varepsilon_r = C\frac{d}{A\varepsilon_0} \tag{9}$$

Where d is the sample thickness, A is the electrode area, C is the measured capacitance, ε_0 is the permittivity of free space (8.854×10^{-12} F/m) [42].

Figures 9A–C and 10A–C illustrate the spectra of relative dielectric permittivity (ε_r) and tangent of the dielectric loss angle (tgδ) for forsterite samples sintered for 2 h at 1400, 1450, and 1500 °C respectively. It is evident from the graph that as the frequency increases, the forsterite sample's relative dielectric constant (ε_r) and tangent of the dielectric loss angle (tgδ) decreases. The combined effects of several

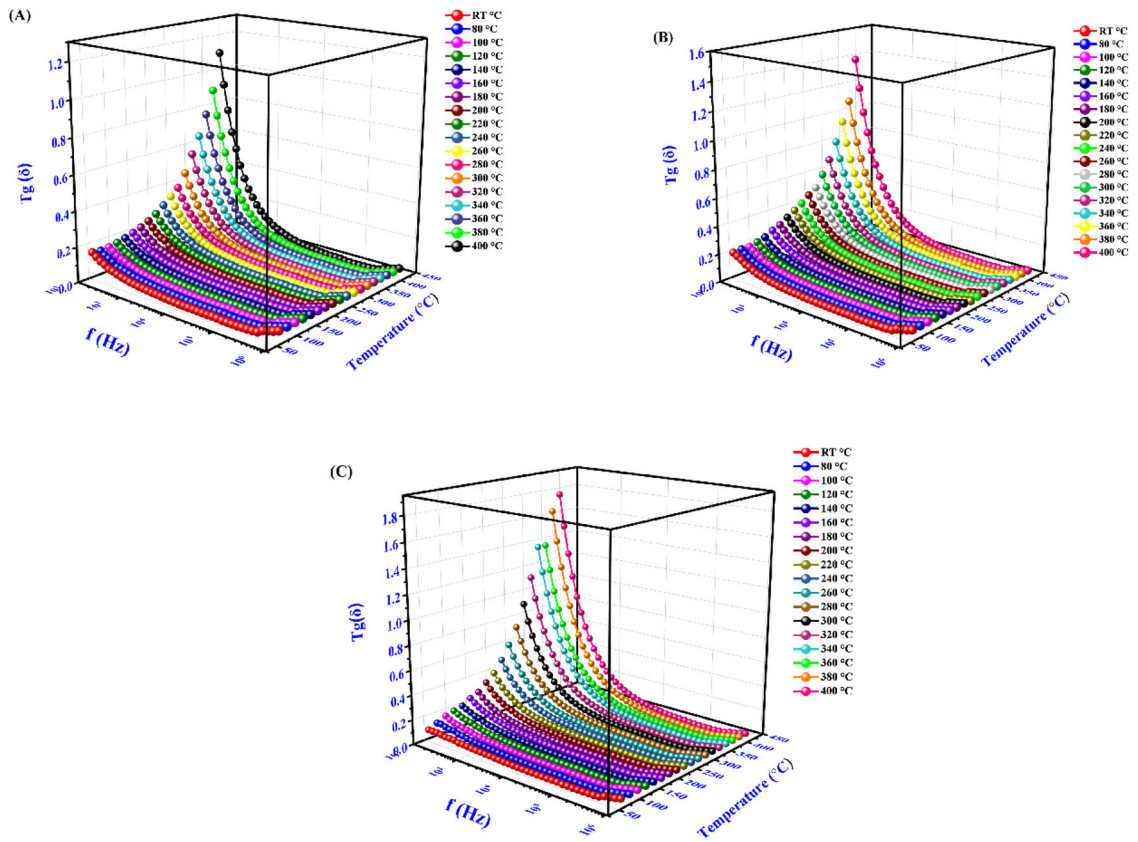

Fig. 10 Tangent of the dielectric loss angle (tgδ) plots at various temperatures for the sintered samples at **A**) 1400, **B**) 1450, and **C**) 1500 °C

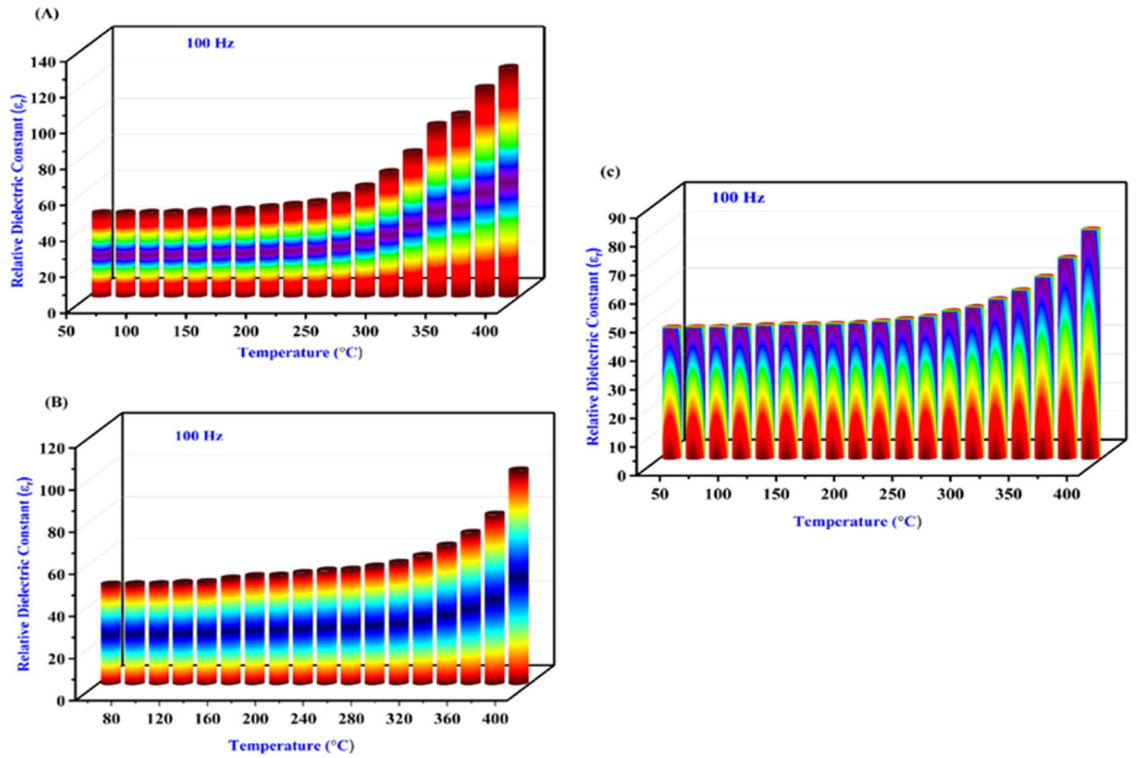

Fig. 11 The temperature dependence of ε_r for the sintered forsterite samples at **A**) 1400, **B**) 1450, and **C**) 1500 °C

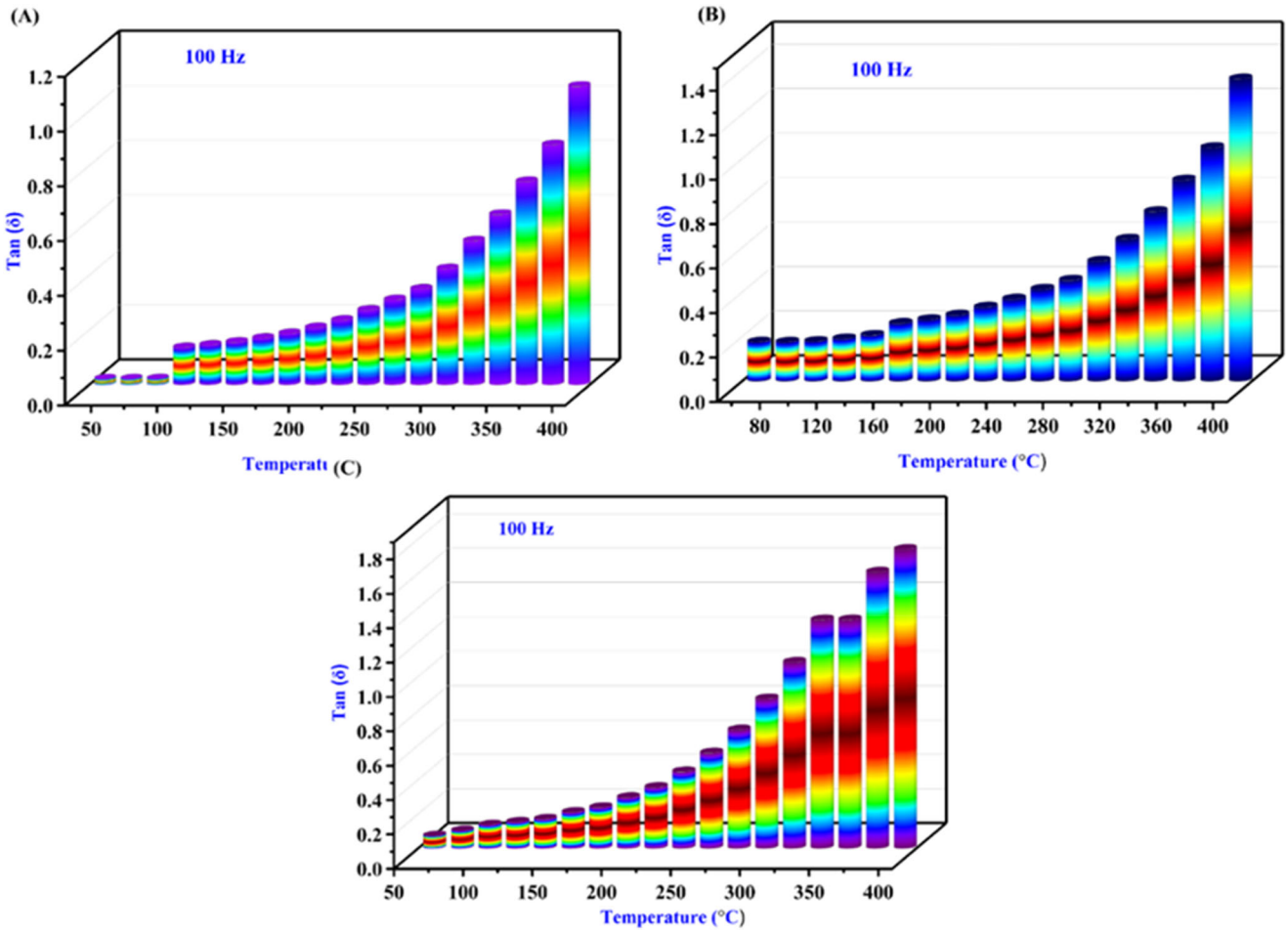

Fig. 12 The temperature dependence of the tangent of the dielectric loss angle (tgδ) for forsterite samples sintered at **A**) 1400, **B**) 1450, and **C**) 1500 °C

types of polarization (atomic, ionic, and electronic) could account for this dielectric trend [1, 32, 43, 44]. Both ε_r and (tgδ) of a forsterite decrease significantly with increasing frequency due to polarization, which reduces the electric field inside a medium [45, 46]. At high frequencies, the (ε_r) attains a steady state low value because of interfacial polarization [33, 47]. Their potential application in multi-functional substrates and electrical components makes their low dielectric constant relevant [48].

3.6.2 Temperature dependent dielectric characterization

Figures 11 and 12 represent the variation of ε_r and tgδ as a function of temperature at 100 Hz for forsterite sintered at 1400, 1450, and 1500 °C for 2 h, respectively. It is evident from the graph that as the temperatures increases, the forsterite sample's relative dielectric constant (ε_r) increases, suggesting that greater temperatures favor dipole orientation, increasing the relative dielectric constant (ε_r) and tangent of the dielectric loss angle (tgδ) values [49–51].

3.7 Electrical modulus spectroscopy

Electrical modulus spectroscopy is a crucial method to discover more about the polarization and relaxation mechanisms generated by electrode effects, grain, and grain boundaries. There are two components to the complex electrical modulus (M*); the real part (M′) and the imaginary part (M″). The following equations provide the formula for the two components of the electrical modulus [52, 53].

$$M^* = M' + jM'' \tag{10}$$

$$\mathbf{M}' = \frac{\boldsymbol{\varepsilon}'}{\left(\boldsymbol{\varepsilon}'^2 + \boldsymbol{\varepsilon}''^2\right)} \tag{11}$$

$$\mathbf{M}'' = \frac{\boldsymbol{\varepsilon}''}{\left(\boldsymbol{\varepsilon}'^2 + \boldsymbol{\varepsilon}''^2\right)} \tag{12}$$

with $\boldsymbol{\varepsilon}'$ and $\boldsymbol{\varepsilon}''$ are the real part and the imaginary part of the dielectric constant for forsterite samples.

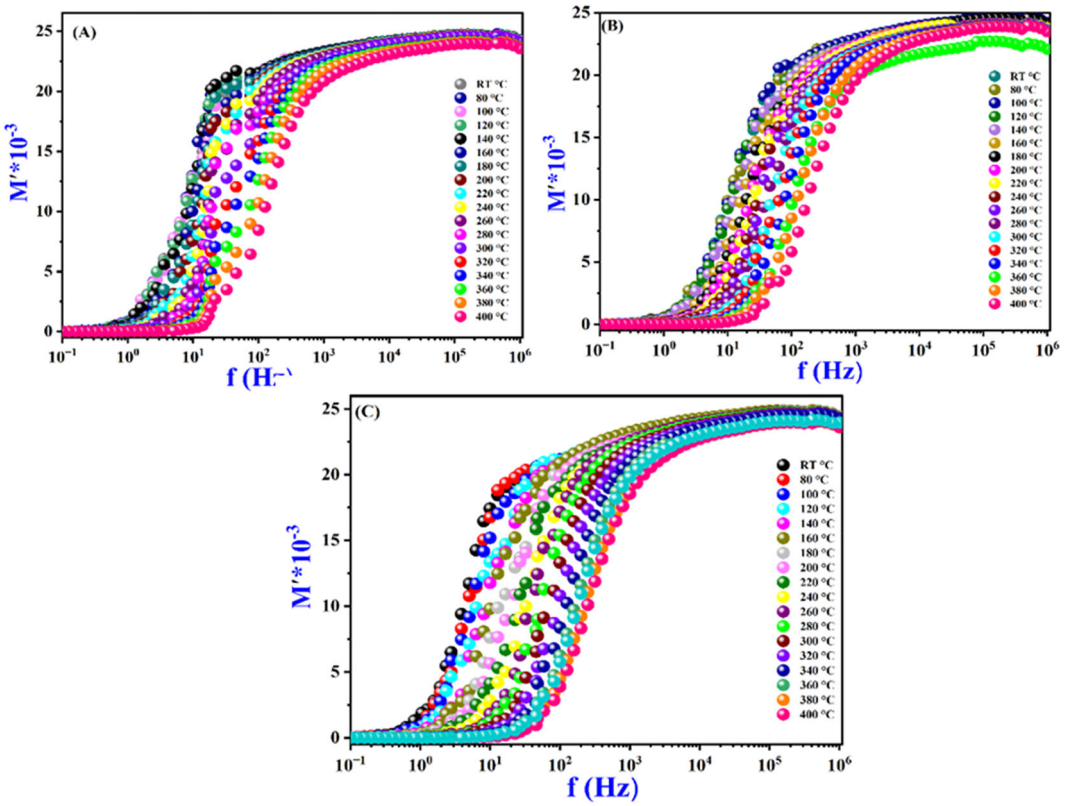

Fig. 13 The frequency dependence of the (M′) at various temperatures for forsterite samples sintered at **A**) 1400, **B**) 1450, and **C**) 1500 °C

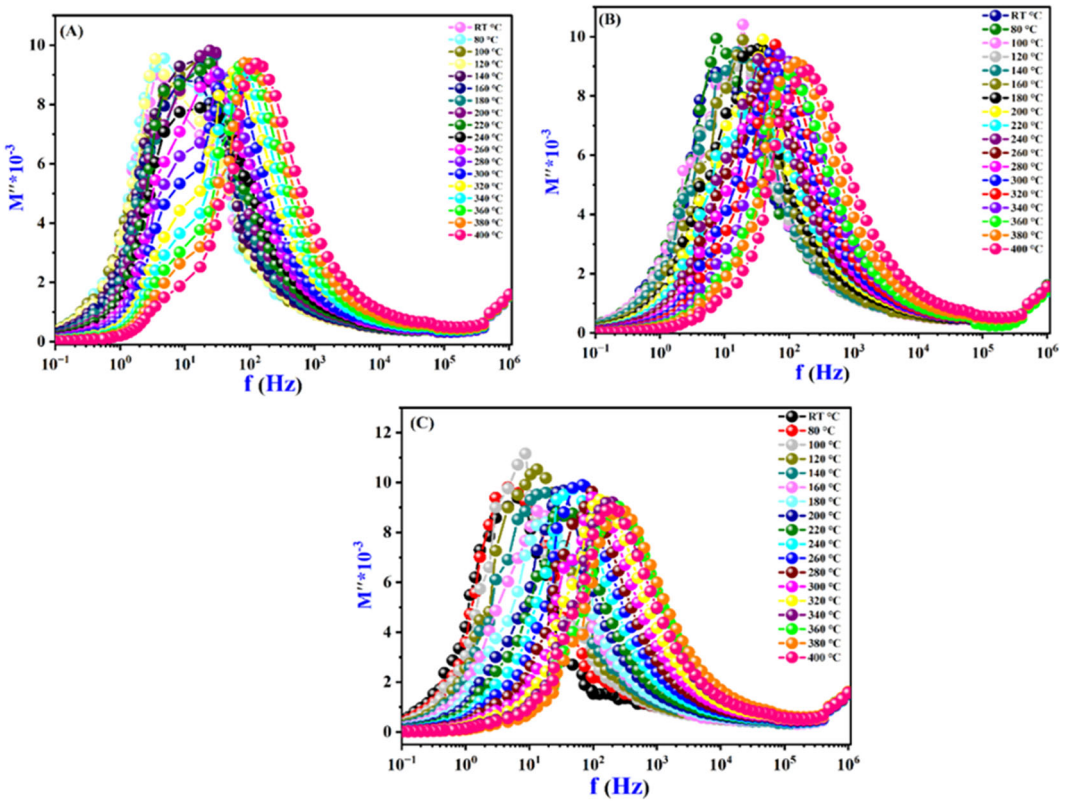

Fig. 14 The frequency dependence of the (M″) at various temperatures for forsterite samples sintered at **A**) 1400, **B**) 1450, and **C**) 1500 °C

The variation in the real part of the electric modulus (M′) with frequency at various temperatures for (Mg_2SiO_4) samples sintered at 1400, 1450, and 1500 °C for 2 h are displayed in Fig. 13A–C. It was noted that at lower-frequency, M′ for all sintered samples is slanted to null at all various temperatures, which indicates that electrode polarization's impact is minimal and insignificant. However, the (M′) exhibited the maximum value at higher frequencies. The conductivity relaxation process could be the source of the dispersion between these frequencies [54, 55]. The phenomenon of continuous dispersion is occurring more frequently, indicating that charge carriers' short-range mobility is limited [56, 57].

Figure 14A–C display the frequency dependence of the imaginary portion of the electric modulus (M″) at different temperatures for forsterite samples sintered at 1400, 1450, and 1500 °C for 2 h. As the temperature rises, the plots show a relaxation peak that shifts towards higher frequencies. The asymmetry noted in the broadening of the relaxation peak implies the dispersion of relaxation time with different time constants, exhibiting the non-Debye type of relaxation in the forsterite samples at 1400, 1450, and 1500 °C for 2 h [57, 58].

4 Conclusions

This work successfully demonstrated the critical influence of sintering temperature on the structural, microstructural, and dielectric properties of forsterite (Mg_2SiO_4) ceramics synthesized via a sol-gel method. XRD analysis confirmed the achievement of phase-pure, highly crystalline orthorhombic forsterite (space group Pbnm) at 1500 °C, while a minor MgO secondary phase persisted at 1400 and 1450 °C and. Microstructural analysis via FESEM revealed a progressive increase in grain size and a significant reduction in open porosity (from ~17% - ~9%) with increasing sintering temperature, leading to enhanced densification and a maximum relative density of 88% at 1500 °C. The electrical and dielectric characterization revealed that the conduction mechanism is governed by hopping charge transport, as described by Jonscher's power law. The dielectric properties were strongly frequency and temperature-dependent, with the low-frequency response dominated by grain boundary effects and interfacial polarization. The observed low dielectric constant and loss tangent across a wide frequency range affirm forsterite's excellent potential for microwave substrate and insulating applications. Ultimately, the optimal sintering temperature was identified as 1500 °C, which yielded the best combination of phase purity, density, microstructural development, and desirable dielectric properties for advanced electronic applications such as high-frequency and microwave device, Sensors and electronic components operating in harsh environments and electronic substrates and packaging materials (biocompatible metallic alloys stainless steel, Ti-alloy, Co–Cr alloys).

Data availability

The data that support the findings of this study are available from the corresponding author upon reasonable request.

Acknowledgements This work was supported by the UK EPSRC (grant QMol EP/X026876/1).

Author contributions A K; methodology, planned and conducted the tests, prepared the manuscript, revised and validated the final manuscript, M H, data analysis and interpretation, prepared the manuscript, revised and validated the final manuscript, L A; data analysis and interpretation, prepared the manuscript, revised and validated the final manuscript, K S E, A I and T A M T; prepared the manuscript, revised and validated the final manuscript, All authors have read and approved the final manuscript version.

Compliance with ethical standards

Conflict of interest The authors declare no competing interests.

Publisher's note Springer Nature remains neutral with regard to jurisdictional claims in published maps and institutional affiliations.

References

1. Asghar G, Dong X, Chae S, Yoo CS, Jeon J, Woo C, Choi JY (2023) Dielectric properties of low-temperature sintered forsterite (Mg_2SiO_4) using high-dispersion and nanoparticle-based solid-state reaction process. Mater Lett 337:134009. https://doi.org/10.1016/j.matlet.2023.134009
2. Asghar G, Dong X, Chae S, Yoo CS, Oh S, Choi KH, Jeon J, Woo C, Kim TY, Ahn J (2022) Synthesis of hollow forsterite by coating method and study of its dielectric properties, Ceram Int. https://doi.org/10.1016/j.ceramint.2022.09.372
3. Keshavarz M, Ebadzadeh T, Banijamali S (2017) Preparation of forsterite/MBS (MgO-B_2O_3-SiO_2) glass-ceramic composites via conventional and microwave assisted sintering routes for LTCC application. Ceram Int 43(12):9259–9266. https://doi.org/10.1016/j.ceramint.2017.04.082
4. Dong H, Liang Y, Nie J, Cai M, Ju M, Li Z, Zhou Y (2023) Synthesis of forsterite with high strength and low acid solubility

using magnesite tailings. Ceram Int 49(8):13258–13264. https://doi.org/10.1016/j.ceramint.2023.01.066
5. Bafrooei HB, Ebadzadeh T, Majidian H (2014) Microwave synthesis and sintering of forsterite nanopowder produced by high energy ball milling. Ceram Int 40(2):2869–2876. https://doi.org/10.1016/j.ceramint.2013.10.025
6. Pratapa S, Handoko WD, Nurbaiti U (2017) Synthesis and characterization of high-density B_2O_3-added forsterite ceramics. Ceram Int 43(9):7172–7176. https://doi.org/10.1016/j.ceramint.2017.03.002
7. Laziri K, Djemli A, Redaoui D, Sahnoune F, Dhahri E, Hassan SF, Saheb N (2024) Kinetics of formation, microstructure, and properties of monolithic forsterite (Mg2SiO4) produced through solid-state reaction of nano-powders of MgO and SiO2. Ceram Int 50(22):45179–45188. https://doi.org/10.1016/j.ceramint.2024.08.357
8. Mohagheghiyan K, Mokhtari H, Kharaziha M (2024) Gelatin-coated mesoporous forsterite scaffold for bone tissue engineering. Ceram Int 50(8):13526–13535. https://doi.org/10.1016/j.ceramint.2024.01.266
9. Soleimani F, Dehghani P (2024) Production of dense forsterite with ultra low dielectric loss using ZrO_2 additive. Ceram Int 50(18):32972–32977. https://doi.org/10.1016/j.ceramint.2024.06.111
10. Mirjalili F, Manafi S, Lotfi F (2020) Examination of morphology, degradation and biocompatibility of fluorapatite–forsterite nanocomposite. Ceram Int 46(13):21256–21267. https://doi.org/10.1016/j.ceramint.2020.05.216
11. Liu Y, Liu P, Hu C (2018) Hydrothermally assisted synthesis of pure-phase and well-dispersed forsterite nanopowders. Ceram Int 44(18):23339–23343. https://doi.org/10.1016/j.ceramint.2018.09.120
12. Ohsato H, Tsunooka T, Sugiyama T et al. (2006) Forsterite ceramics for millimeterwave dielectrics. J Electroceram 17:445–450. https://doi.org/10.1007/s10832-006-0452-6
13. Saberi A, Alinejad B, Negahdari Z, Kazemi F, Almasi A (2007) A novel method to low temperature synthesis of nanocrystalline forsterite. Mater Res Bull 42(4):666–673. https://doi.org/10.1016/j.materresbull.2006.07.020
14. Liu Y, Liu P, Hu C (2018) Hydrothermally assisted synthesis of pure-phase and well- dispersed forsterite nanopowders. Ceram Int 44(18):23339–23343. https://doi.org/10.1016/j.ceramint.2018.09.120
15. Maghsoudlou MSA, Ebadzadeh T, Sharafi Z, Arabi M, Zahabi KR (2016) Synthesis and sintering of nano-sized forsterite prepared by short mechanochemical activation process. J Alloy Compd 678:290–296. https://doi.org/10.1016/j.jallcom.2016.02.020
16. Temuujin J, Okada K, MacKenzie K (1998) Role of water in the mechanochemical reactions of MgO–SiO_2 systems. J Solid State Chem 138(1):169–177. https://doi.org/10.1006/jssc.1998.7768
17. Alkathy MS, Hezam A, Manoja KSD, Wang J, Cheng C, Byrappa K, Raju KJ (2018) Effect of sintering temperature on structural, electrical, and ferroelectric properties of lanthanum and sodium co-substituted barium titanate ceramics. J Alloy Compd 762:49–61. https://doi.org/10.1016/j.jallcom.2018.05.138
18. Sharma A, Singh M, Kishore K, Pathak D, Batoo KM, Qaisar T, Lal M (2025) Influence of low sintering temperature on the structural, morphological, and dielectric properties of $(Bi_{0.4}Ba_{0.1})Na_{0.5}TiO_3$ ceramics. J Mater Sci Mater Electron 36(6):392
19. Soleimani F, Afghahi SSS, Dehghani P (2025). Synthesis and sintering of forsterite with high quality factor through quartzing and precise control of phase values. Ceramics Int. https://doi.org/10.1016/j.ceramint.2025.06.229
20. Ghelloudj E, & Keziz A (2025) Experimental failure analysis of AISI 4140 steel interconnecting shaft of the high-speed centrifugal compressor for regeneration gas. Eng Failure Anal, 109283. https://doi.org/10.1016/j.engfailanal.2025.109283.
21. Kherifi D, Keziz A, Rasheed M, & Oueslati A (2024) Thermal treatment effects on Algerian natural phosphate bioceramics: A comprehensive analysis. Ceramics Int. https://doi.org/10.1016/j.ceramint.2024.05.317.
22. Keziz A, Heraiz M, Sahnoune F et al. (2023) Dense, Hard, and Thermally Stable $Al_6Si_2O_{13}$–$Mg_2Al_4Si_5O_{18}$ Composite Material for Silicon Substrate Applications. Silicon 15:4675–4688. https://doi.org/10.1007/s12633-023-02373-y
23. Keziz A, Heraiz M, Sahnoune F, Rasheed M (2023) Characterization and mechanisms of the phase's formation evolution in sol-gel derived mullite/cordierite composite. Ceram Int 49(20):32989–33003. https://doi.org/10.1016/j.ceramint.2023.09.068
24. Saheb N (2014) Sintering behavior of CNT reinforced Al6061 and Al2124 nanocomposites. Adv Mater Sci Eng 2014:9. https://doi.org/10.1155/2014/535640
25. Sánchez-Soto PJ, Eliche-Quesada D, Martínez-Martínez S, Garzón-Garzón E, Pérez-Villarejo L, Rincón JM (2018) The effect of vitreous phase on mullite and mullite-based ceramic composites from kaolin wastes as by-products of mining, sericite clays and kaolinite. Mater Lett 223:154–158
26. Peng Z-H, Zheng D-Y, Zhou T, Yang L, Zhang N, Fang C (2018) Effects of Co_2O_3 doping on electrical properties and dielectric relaxation of PMS–PNN–PZT ceramics. J Mater Sci Mater Electron 29(7):5961–5968. https://doi.org/10.1007/s10854-018-8569-3
27. Bouferra R, Marín G, Amhil S, Wasim SM, Essaleh L (2019) Low temperature electrical impedance spectroscopy characterization of n type $CuInSe_2$ semiconductor compound. Phys B Condens Matter 565:14–17. https://doi.org/10.1016/j.physb.2019.04.028
28. Assoudi N, Chaabani A, Rasheed M, Walha I, Dhahri E, Alawsi T, Barille R (2022) Comparative examination of the physical parameters of the sol gel produced compounds $La_{0.5}Ag_{0.1}Ca_{0.4}MnO_3$ and $La_{0.6}Ca_{0.3}Ag_{0.1}MnO_3$. Opt Quantum Electron 54(9):556. https://doi.org/10.1007/s11082-022-03927-x
29. Gouti I, García-Granda S, Litaiem H (2021) Electrical and dielectric investigation, thermal analysis and vibrational spectroscopic study on the new hydrogeno–arsenate tellurate conductor. Mater Sci Eng, B 265:114981
30. Mahani RM, Omara S (2019) Grain and grain boundaries contributions to dielectric relaxation of the clay-based ceramics. Appl Phys A 125(8):573
31. Chérif SF, Chérif A, Dridi W, Zid MF (2020) Ac conductivity, electric modulus analysis, dielectric behavior and Bond Valence Sum analysis of $Na_3Nb_4As_3O_{19}$ compound. Arab J Chem 13(6):5627–5638
32. El Asri S, El Hadri M, Rahim MA, Essaleh L, Ahamdane H, Hajji L, Mansori M (2022) Structural, microstructure and ac impedance spectroscopy investigation of parent and M-doped forsterite $Mg_{1.9}M_{0.1}SiO_4$ (M= Co, Ni and Mn). Phys B Condens Matter 643:414127. https://doi.org/10.1016/j.physb.2022.414127
33. Karbovnyk I, Borshchyshyn I, Vakhula Y, Lutsyuk I, Klym H, Bolesta I (2016) Impedance characterization of Cr^{3+}, Y^{3+} and Zr^{4+} activated forsterite nanoceramics synthesized by sol–gel method. Ceram Int 42(7):8501–8504. https://doi.org/10.1016/j.ceramint.2016.02.075
34. Nouri F, Trabelsi-Ayadi M (2022) Riadh Ternane, Synthesis and ionic conductivity of phosphate-sulfate fluorapatites $Ca_{10-x}Na_x(PO_4)_{6-x}(SO_4)_xF_2$ (x=0, 3, 6). Mater Sci Eng B 282:115786–115786. https://doi.org/10.1016/j.mseb.2022.115786
35. Messai B, Makhloufi R, Keziz A, Benmakhlouf A, Nouiri M, & Taha TAM (2025). Integrated Study of Morphology, Structure, and Dielectric Behavior in PZT-SASF Ceramics at the Morphotropic Phase Boundary. Ceramics International.

36. Keziz A, Rasheed M, Heraiz M, Sahnoune F, Latif A (2023) Structural, morphological, dielectric properties, impedance spectroscopy and electrical modulus of sintered $Al_6Si_2O_{13}$–$Mg_2Al_4Si_5O_{18}$ composite for electronic applications. Ceram Int 49(23):37423–37434. https://doi.org/10.1016/j.ceramint.2023.09.068
37. Djelel K, Keziz A, Rasheed M, Oueslati A (2025) SiO_2's influence on the dielectric properties of natural fluorapatite-derived bio-compounds. Ceramics Int 51(7):8658–8673. https://doi.org/10.1016/j.ceramint.2024.12.296
38. Keziz A, Heraiz M, Rasheed M, Oueslati A (2024) Investigating the dielectric characteristics, electrical conduction mechanisms, morphology, and structural features of mullite via sol-gel synthesis at low temperatures. Mater Chem Phys 325:129757. https://doi.org/10.1016/j.matchemphys.2024.129757
39. Athokpam S, Madolappa S, Fernandes BJ, Ramesh K, Ramesh KP, & Mallikarjunaiah KJ (2025). Electrical conductivity and dielectric study of zinc substituted tellurovanadate glass systems. Ceramics Int. https://doi.org/10.1016/j.ceramint.2025.03.016
40. Tayari F, Nassar KI, Benamara M, Essid M, Teixeira SS, Graça MPF (2024) Sol–gel synthesized $(Bi_{0.5}Ba_{0.5}Ag)_{0.5}(NiMn)_{0.5}O_3$ perovskite ceramic: An exploration of its structural characteristics, dielectric properties and electrical conductivity. Ceram Int 50(7):11207–11215. https://doi.org/10.1016/j.ceramint.2024.01.022
41. Dhifallah N, Hehlen B, Khemakhem H (2022) Electrical conductivity and impedance spectroscopy studies of ceramic $(Ba_{0.8}Sr_{0.2})$ $Ti_{0.95}(Zn_{1/3}Nb_{2/3})_{0.05}O_3$ doped with Bi_2O_3. Solid State Commun 358:115003. https://doi.org/10.1016/j.ssc.2022.115003
42. Benmakhlouf A, Makhloufi R, Boutarfaia A, Messai B, Hadji F, & Nouiri M (2023). The effect of Barium substitution on the structural and dielectric properties of $Pb_{1-X}Ba_X(Zr_{0.52}Ti_{0.43}(Al_{0.5}Sb_{0.5})_{0.05})O_3$ ceramics at the morphotropic phase boundary. J Ovonic Res, 19(3)
43. Li J-H, Wang S-F, Hsu Y-F, Chung T-F, Yang J-R (2018) "Effects of Sc_2O_3 and MgO additions on the dielectric properties of $BaTiO_3$-based X8R materials". J Alloy Compd 768:122–129. https://doi.org/10.1016/j.jallcom.2018.07.196
44. Kaliyaperumal C, Sankarakumar A, Paramasivam T (2020) Grain size effect on the electrical properties of nanocrystalline $Gd_2Zr_2O_7$ ceramics. J Alloy Compd 813:152221. https://doi.org/10.1016/j.jallcom.2019.152221
45. Sasikala TS, Suma MN, Mohanan P, Pavithran C, Sebastian MT (2008) Forsterite-based ceramic–glass composites for substrate applications in microwave and millimeter wave communications. J Alloy Compd 461(1-2):555–559. https://doi.org/10.1016/j.jallcom.2007.07.084
46. Saîd S, Didry S, El Amrani M, Autret-Lambert C, Megriche A (2018) Brilliant effect of Ni substitution in the appearance of high dielectric constant in $CaCu_{2.9}Ni_{0.1}Ti_{3.9}Ni_{0.1}O_{12}$ ceramics. J Alloy Compd 765:927–935. https://doi.org/10.1016/j.jallcom.2018.06.282
47. Wang XH, Chen RZ, Gui ZL, Li LT (2003) The grain size effect on dielectric properties of $BaTiO_3$ based ceramics. Mater Sci Eng B 99(1-3):199–202. https://doi.org/10.1016/S0921-5107(02)00520-2
48. Majumder SB, Bhattacharyya S, Katiyar RS, Manivannan A, Dutta P, and Seehra MS, Dielectric and magnetic properties of sol-gel-derived lead iron niobate ceramics, 99, 2, 024108–024108, 2006, https://doi.org/10.1063/1.2158131
49. Kool A, Thakur P, Bagchi B, Hoque NA, Banerjee S, Das S (2015) "Sol–gel synthesis of transition-metal ion conjugated alumina-rich mullite nanocomposites with potential mechanical, dielectric and photoluminescence properties". RSC Adv 5(no. 126):104299–104313. https://doi.org/10.1039/c5ra21091g
50. Carvalho RS, da Silva B, Lira HL, Santana (2020) Fabrication and characterization of dielectric ceramics using alumina and aluminosilicates. Cerâmica 66(no. 377):56–64. https://doi.org/10.1590/03666913202066377280 8
51. S Labihi, A Eddiai, M El Achaby, M Rguiti, and M Mazroui, A study on the enhancement in β-phase and dielectric properties of BCZT lead-free reinforced in PVDF-HFP nanocomposite thick films for eco-friendly energy harvesting, Ceramics Int. 2024, https://doi.org/10.1016/j.ceramint.2024.07.363
52. Smii S, Moualhi Y, Bahri F, Rahmouni H (2023) Electrical transport phenomena and modulus behavior in lead-free $Ba_{0.85}Sr_{0.15}Ti_{0.85}Zr_{0.15}O_3$ compound. Phys B Condens Matter 662:414966. https://doi.org/10.1016/j.physb.2023.414966
53. Singha A, Praharaj S, & Rout D (2025). In situ Raman and electric modulus study of NBT-ST-KNN ceramics: An insight into temperature evolution of relaxor dynamics. Mater Res Bull, 113534. https://doi.org/10.1016/j.materresbull.2025.113534
54. Chen X, Zhou F, Gao J, & Song X (2025) Structure, electrical properties, and electrical modulus of $Ce_{0.98-x}(Gd_{1/2}Sm_{1/2})_xCa_{0.02}O_{2-\delta}$ ceria electrolytes sintered by microwave. J Solid State Chem. 125456. https://doi.org/10.1016/j.jssc.2025.125456
55. Meena R, Dhaka RS (2024) Temperature dependent conductivity, dielectric relaxation, electrical modulus and impedance spectroscopy of Ni substituted $Na_{3+2x}Zr_{2-x}Ni_xSi_2PO_{12}$. Phys B Condens Matter 690:416209. https://doi.org/10.1016/j.physb.2024.416209
56. Thomas AK, Abraham K, Thomas J, Saban KV (2017) Electrical and dielectric behaviour of $Na_{0.5}La_{0.25}Sm_{0.25}Cu_3Ti_4O_{12}$ ceramics investigated by impedance and modulus spectroscopy. J Asian Ceram Soc 5(1):56–61. https://doi.org/10.1016/j.jascer.2017.01.002
57. Mahmood MF, Hossen MB (2024) Rietveld refinement and complex dielectric, modulus and impedance study of $Ni_{0.27}Cu_{0.10}Zn_{0.63}Al_xFe_{2-x}O_4$ bulk ceramics. Results Phys 62:107833. https://doi.org/10.1016/j.rinp.2024.107833
58. Tirupathi P, Sekhar KC, Mahesh MLV, Saini DS, Rayaprol S, Babu PD (2025) Structural, electrical, impedance, and modulus correlation in magnetoelectric multiferroic properties of Sm-doped Nb^{5+} & Co/Fe substitution in $Bi_5Ti_4O_{15}$; n=4 layered Aurivillius. J Alloy Compd 1014:178788. https://doi.org/10.1016/j.jallcom.2025.178788